Detection and imaging of quorum sensing in *Pseudomonas aeruginosa* biofilm communities by surface-enhanced resonance Raman scattering

Gustavo Bodelón,[a,*] Verónica Montes-García,[a] Vanesa López-Puente,[a] Eric H. Hill,[b] Cyrille Hamon,[b] Marta N. Sanz-Ortiz,[b] Sergio Rodal-Cedeira,[a] Celina Costas,[a] Sirin Celiksoy,[a] Ignacio Pérez-Juste,[a] Leonardo Scarabelli,[b] Andrea La Porta,[b] Jorge Pérez-Juste,[a] Isabel Pastoriza-Santos[a] and Luis M. Liz-Marzán[a,b,c,d,*]

[a] Departamento de Química Física, Universidade de Vigo, 36310 Vigo, Spain

[b] Bionanoplasmonics Laboratory, CIC biomaGUNE, Paseo de Miramón 182, 20009 Donostia-San Sebastián, Spain

[c] Ikerbasque, Basque Foundation for Science, 48013 Bilbao, Spain

[d] Biomedical Research Networking Center in Bioengineering, Biomaterials, and Nanomedicine (CIBER-BBN), Spain

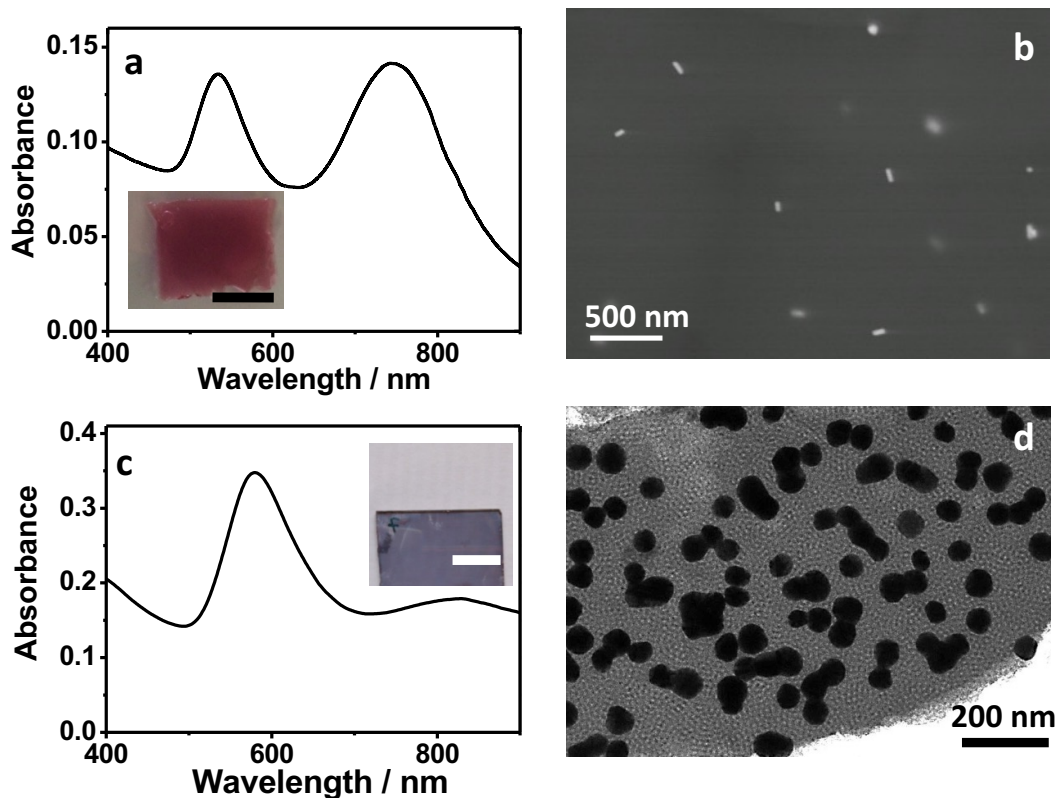# Section S1. Plasmonic substrates: synthesis and characterization

Figure S1.1. Characterization of plasmonic substrates. a) Representative Vis-NIR spectrum of pNIPAM hydrogels doped with gold nanorods in the swollen state. The inset shows a photograph of the doped hydrogel, the scale bar represents 0.5 cm. **b**) Representative SEM image of the Au-doped hydrogel showing the homogenous distribution of gold nanorods. **c**) Vis-NIR spectrum of the Au@TiO$_2$ thin film (a photograph is presented in the inset, the scale bar represents 0.5 cm). **d**) Representative TEM micrograph of the Au@TiO$_2$ nanocomposite.
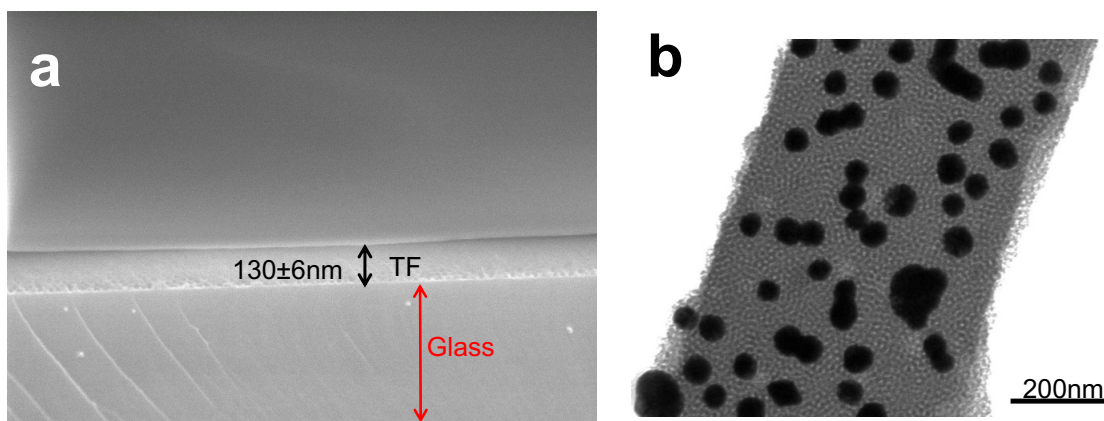
Figure S1.2. Structural characterization of Au@TiO$_2$ nanocomposites. a) Cross-section SEM image of an Au@TiO$_2$ thin film showing an average thickness of 130 ± 6 nm. **b**) Representative TEM micrograph of the Au@TiO$_2$ thin film.
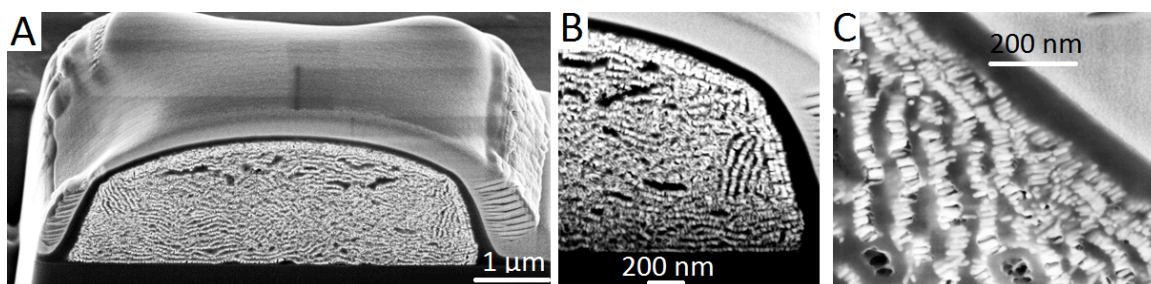

Figure S1.3. Structural characterization of Au@SiO$_2$ nanorod supercrystals. (A-C) Cross-section SEM images (after FIB processing) at different magnifications of an Au@SiO$_2$ nanorod supercrystal showing the internal nanorod organization and the mesoporous silica in between nanorod monolayers.

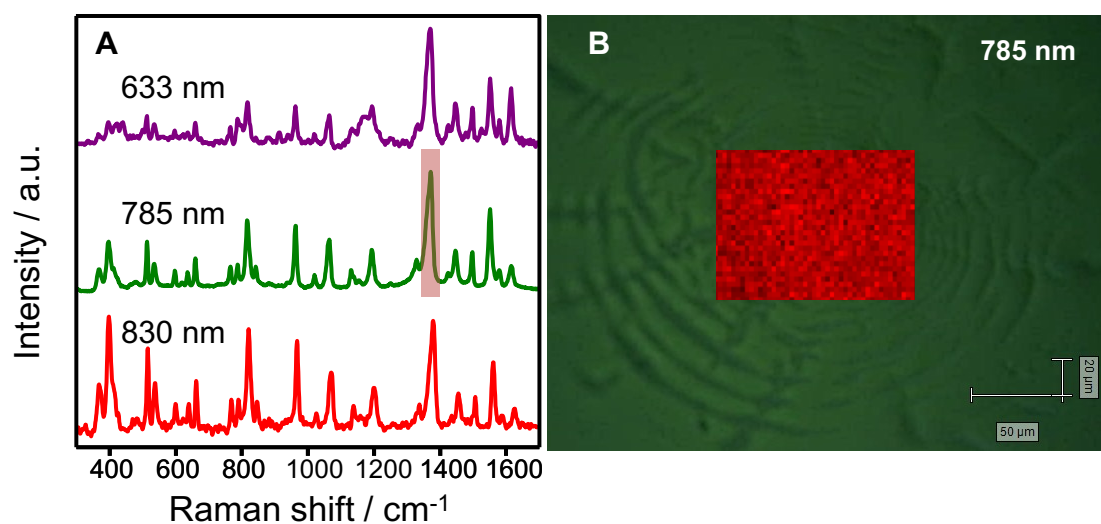# Section S2. Analysis of the SERS performance of the plasmonic substrates

Figure S2.1. SERS characterization of Au@pNIPAM hydrogels using 1- naphthalenethiol, 1-NAT as Raman active probe. SERS spectra of 1-NAT on Au@pNIPAM hydrogel at three different excitation lines (633, 785, 830 nm) as indicated. (B) Superimposed optical image and SERS mapping of the hydrogel. The SERS mapping was performed at 1371 cm^{-1} with 785nm excitation line, 20× objective and a maximum power of 5.9mW. Acquisition time 0.1s.
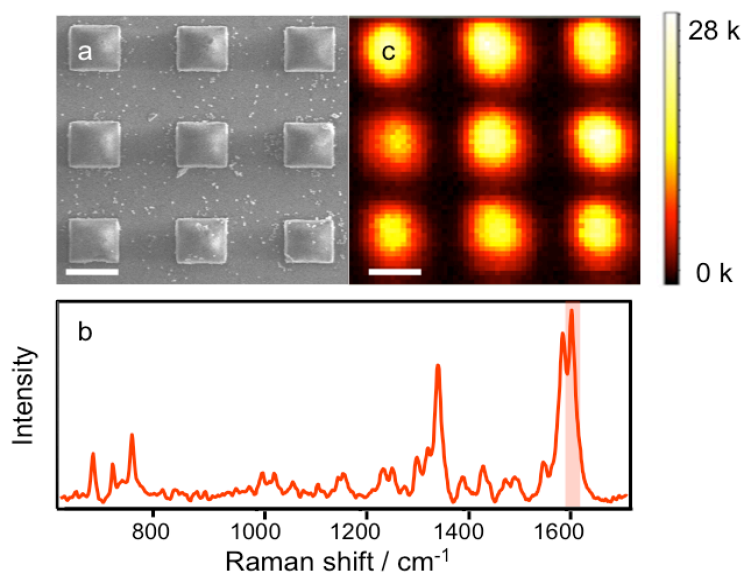
Figure S2.2. SERS characterization of Micropatterned Au@SiO₂ supercrystal arrays. a) SEM image of silica-coated Au nanorod supercrystals. Scale bar is 10 μm. **b)** Representative SERRS spectrum and **c)** graphical representation of SERRS intensity mapping (1600 cm^{-1}) of commercial pyocyanin (10^{-7} M) performed using 785 nm laser line, 50× objective and a maximum power of 11.34 mW for measurements in the wet state (1.5 mW if dry). Acquisition time was 0.1s. Scale bar: 10 μm. Intensity scale bar (kcts/mWs).

Section S3. Computational Methods. UV-Visible-NIR and Raman Spectroscopic characterization of Phenazines

The optimized geometry and Raman spectra of pyocyanin have been obtained theoretically using the B3LYP/6-31G* density functional method (DFT) and the Gaussian09 program.[1] Vibrational assignments were aided by using the VEDA program, which generates an optimized set of internal coordinates based on the molecular structure and provides a potential energy distribution for the quantitative analysis of vibrational spectra.[2] TDDFT computations with different basis sets have been performed to improve the agreement between theoretical an experimental data and the influence of the solvent (water) has been taken into account using the Polarizable Continuum Model (PCM) as included in Gaussian09.
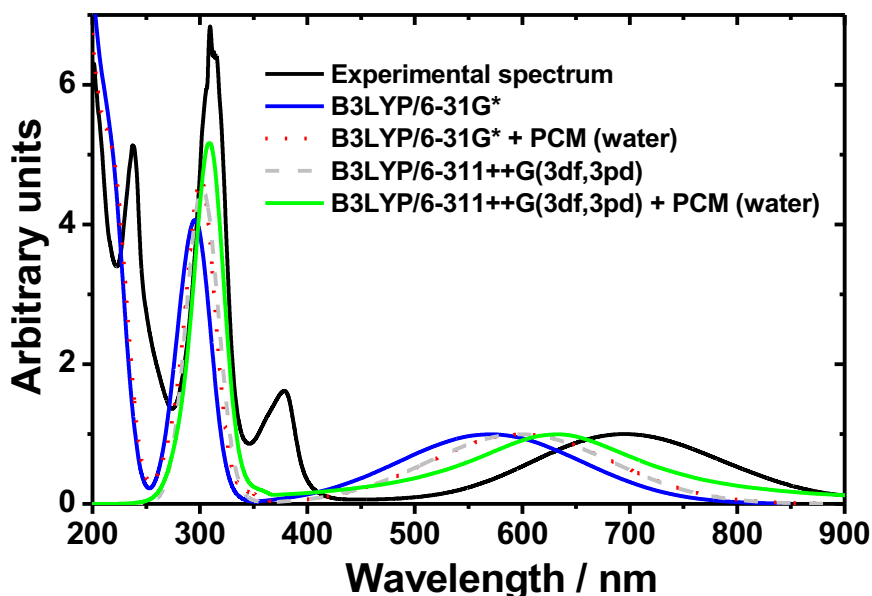

Figure S3.1 Experimental and theoretical absorption spectra of pyocyanin. The theoretical spectra were computed with several basis sets in gas phase and solution (PCM). All spectra were normalized to unity at the maximum of the band located at the higher wavelength (see Table S3.1 below for details).

Theoretical UV-Vis-NIR spectra of pyocyanin are always blue-shifted respect to the experimental data (see Fig. S3.1 and Table S3.1). Despite these differences, all the theoretical methods employed agree in predicting that the band at higher wavelength, corresponding to the experimental band at 695 nm, is originated by a $\pi \rightarrow \pi^*$ transition between the HOMO-LUMO orbitals.

Table S3.1. Theoretical methods employed to obtain the UV-Vis-NIR spectra of pyocyanin as well as the band position at the higher wavelength. The experimental value of this transition is also included.

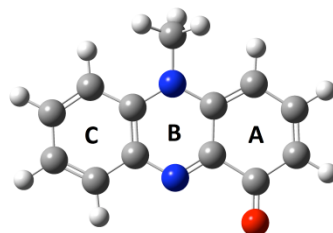| Theoretical method	λ_{max} / nm
B3LYP/6-31G*	570.2
B3LYP/6-31G* + PCM (water)	598.8
B3LYP/6-311++G(3df,3pd)	597.8
B3LYP/6-311++G(3df,3pd) + PCM (water)	631.2
Experimental spectrum	695
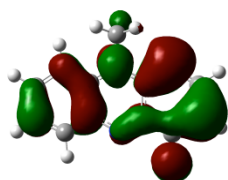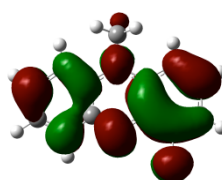
HOMO   LUMO

Table S3.2. Experimental and calculated vibrational frequencies (cm^{-1}) of pyocyanin and corresponding assignments.

Raman	Calculated	Description	Potential energy distribution
413	407	Ring deformations (aprox. in-plane)	37% ring (B) CCN bendings + 10% C-N stretchings
498	504	Ring deformations (out-of-plane)	15% ring (B) CCCN torsion + 11% CC=O bending
519	520	Ring deformations (aprox. in-plane)	59% ring (A,B) CCC and CCN bendings
547	543	Ring deformations (aprox. in-plane)	39% ring (A,C) CCC bendings + 13% ring (B) CNC bending
595	600	Ring deformations (aprox. in-plane)	16% ring (A,B,C) CCC and CCN bendings + 15% CC=O bending
638	638	Ring deformations (aprox. in-plane)	52% ring (A,B,C) CCC and CCN bendings
676	690	Ring deformations (aprox. in-plane)	39% ring (A,C) CCC bendings + 11% ring (B) C-N stretchings
814	810	Ring deformations (out-of-plane)	38% ring (A) CCCH torsion + 11% ring (B) CCNC torsion
842	850	Ring deformations (aprox. in-plane)	48% ring (A,C) CCC bendings and ring (B) CCN bendings
880	862	Ring deformations (out-of-plane)	72% ring (C) CCCH torsion
896	902	Ring deformations (aprox. in-plane)	54% ring (A,C) CCC bendings
987	1001	Ring stretchings	27% N-C$_{Me}$ ring stretching
1074	1067	Ring stretchings	58% ring (C) C=C stretching + 11% CH$_3$ bending
1092	1081	Ring stretchings	47% ring (A) C=C stretching + 21% ring (A) CH bending
1173	1153	N-CH$_3$ wagging	33% CH$_3$ torsion + 15% ring (A,C) CH bending + 13% CH$_3$ bending
1185	1197	Ring CH bendings	51% ring (A,C) CH bending

The RMS error for this assignation is 15.5 cm^{-1}

Table S3.2 (continued). Experimental and calculated vibrational frequencies (cm^{-1}) of pyocyanin and corresponding assignments.
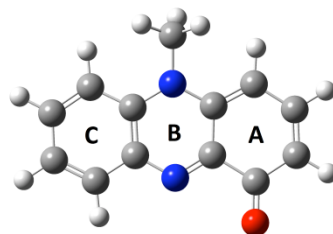
| Raman	Calculated	Description	Potential energy distribution
1266	1252	Ring stretchings and ring CH bendings	22% ring (A) C=C stretching + 13% ring (A) CH bending
1290	1292	Ring stretchings	31% ring (B) C=N stretch + 15% ring (C) C=C stretching
	1315	Ring CH bendings	25% ring (C) CH bending + 13% ring (C) C=C stretching
	1327	Ring stretchings	46% ring (B) C-N streching + 13% ring (A) CH bending
1356	1364	Ring stretchings	36% ring (C) C=C stretching + 18% ring (B) C-N stretching + 10% CH$_3$ bending
	1379	Ring stretchings	23% ring (B) C-N stretching + 12% ring (C) C=C stretching
1406	1419	Ring CH bendings	40% ring (A) CH bending
	1459	Ring CH bendings	37% ring (A) CH bending + 12% ring (A) C=C stretching
1468	1482	CH$_3$ wagging	80% CH$_3$ bending
1489	1504	CH$_3$ scissoring and ring CH bendings	27% ring (A) CH bending + 18% ring (B) C=C stretching + 10% CH$_3$ bending
1517	1513	CH$_3$ scissoring and ring CH bendings	42% CH$_3$ bending
1565	1543	CH$_3$ scissoring	66% CH$_3$ bending + 15% CH$_3$ torsion
1606	1578	Ring stretchings	64% ring (A) C=C stretching
1619	1593	Ring stretchings	40% ring (B) C=N stretching
	1621	Ring stretchings	32% ring (C) C=C stretching + 10% ring (B) C=N stretching
	1656	Ring stretchings	55% ring (A,C) C=C stretching
	1671	Ring stretchings	55% ring (A,C) C=C stretching + 10% C=O stretching
	1739	C=O stretching	70% C=O stretching
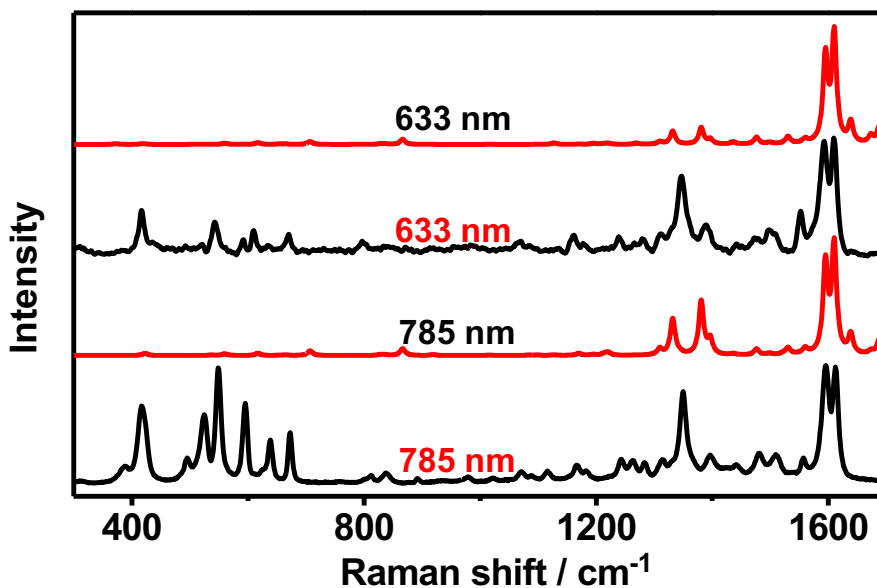
Figure S3.2. Theoretical Raman (red) and experimental Resonant Raman (black) spectra of pyocyanin obtained at the indicated excitation wavelengths.

As can be seen in Fig. S3.2, the theoretical Raman spectra of pyocyanin obtained with excitation wavelengths at 633 and 785 nm agree reasonably well with the experimental resonance Raman (RR) spectra. According to the vibrational assignments in Table S3.1, the RR spectrum of pyocyanin is dominated by three aromatic ring stretchings at 1356, 1606 and 1619 cm^{-1}), followed by a group of signals between 407 and 690 cm^{-1} associated to different ring deformations (signals marked in blue in Table S3.2).

However, the relative intensities of both groups of bands change markedly with the excitation wavelength. It is known that RR intensities obtained with excitation wavelengths close to the absorption maximum depend mainly on the Franck-Condon overlap integrals,[3] so that those vibrational normal modes with different geometries in the ground and excited states are expected to be more intense. As can be seen from the molecular orbitals depicted in Figure S3.1 the excitation around 590 nm populates the π^* molecular orbital and many of the C-C and C-N bonds of the aromatic system would increase their length in the excited state. As a consequence, the bands at 1356, 1606 and

1619 cm^{-1} assigned to the molecular skeleton stretching modes originate strong RR bands. On the other hand, from previous studies on R6G it has been stated that for aromatic systems with Raman excitation profiles similar to the absorption spectrum, the RR intensity of the bending modes decreases less than those of the stretching modes when using excitation wavelengths red-shifted with respect to the absorption maximum.[4] Furthermore, since the geometry in aromatic systems does not change significantly for bending vibrations, it has been suggested that ring bending modes (those between 400 and 690 cm^{-1}) would obtain their RR intensity by a different mechanism (vibronic coupling) which involves molecular orbitals of higher energy transitions. According to all the previous, the RR spectrum at 633 nm is dominated by the ring stretching signals at 1356 and 1610 cm^{-1} because their intensities are determined by Franck-Condon factors. Under excitation at 785 nm both stretching and bending modes show more similar RR intensities, because there is a decrease in RR intensity when moving to the red of the absorption maximum, but the reduction is less pronounced in the bending modes (gaining intensity by vibronic coupling) and in the strecthing mode at 1356 cm^{-1}. These trends can be observed in the experimental and theoretical spectra, although the intensity changes for the bending modes are not so well reproduced/evident in the theoretical profiles. Finally, it must be also noted that the SERRS spectra are quite similar to the RR profiles (see Figure 2 in the main text), which suggests that the same factors determining RR intensity are the main responsible ones for the SERRS intensities.

UV-Vis-NIR characterizacion of extracted phenazines from bacterial cultures. The biosynthetic pathways for phenazine production in *Pseudomonas aeruginosa* PA14 produces at least five types of phenazines from phenazine-1-carboxylic acid (PCA), which can be converted into 1-hydroxyphenazine (1-HO-PHZ), phenazine-1-carboxamide (PCN), 5-methylphenazine-1-carboxylic acid betaine (5-MCA) and

pyocyanin, by action of the enzymes PhzS, PhzH, and PhzM (see Fig. S4.1 in the supporting information for details). We characterized the optical properties of the different phenazines in water (after their extraction from bacterial cultures with chloroform, as described in Section S4).

Figure S3.3 shows that, although all molecules share the same phenazine ring chromophore, the optical properties of their corresponding solutions are very different. In fact, only the wild type PA14 and the mutant PhzH show a broad absorption band in the visible-NIR region (550 to 900 nm) corresponding to pyocyanin, while the other mutants (PhzS and PhzH) show absorption bands in the UV region, which are characteristic of the other phenazines.[5] These results thus confirm that only pyocyanin can display a Resonant Raman scattering contribution at the excitation wavelengths used in this study (633 and 785 nm).
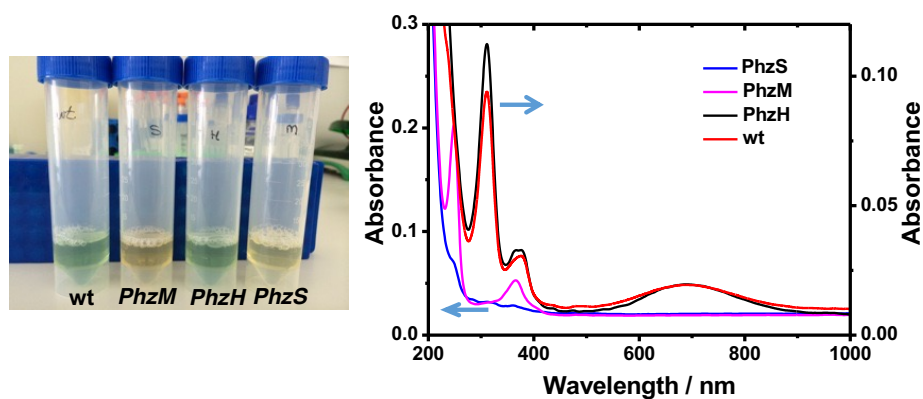

Figure S3.3. Left: Photographs of the phenazine-containing samples obtained from the *wild type* PA14 (wt) and the different mutants (PhzH, PhzS and PhzM), as labeled, under visible light illumination. Right: UV-Vis-NIR spectra of the samples containing different phenazines; pyocyanin (wt and PhzH), 1-hydroxyphenazine (1-HO-PHZ, wt, PhzM and PhzH) and phenazine-1-carboxamide (PCN, wt, PhzS and PhzM).

Section S4. Plasmonic detection of pyocyanin in planktonic and biofilm cultures
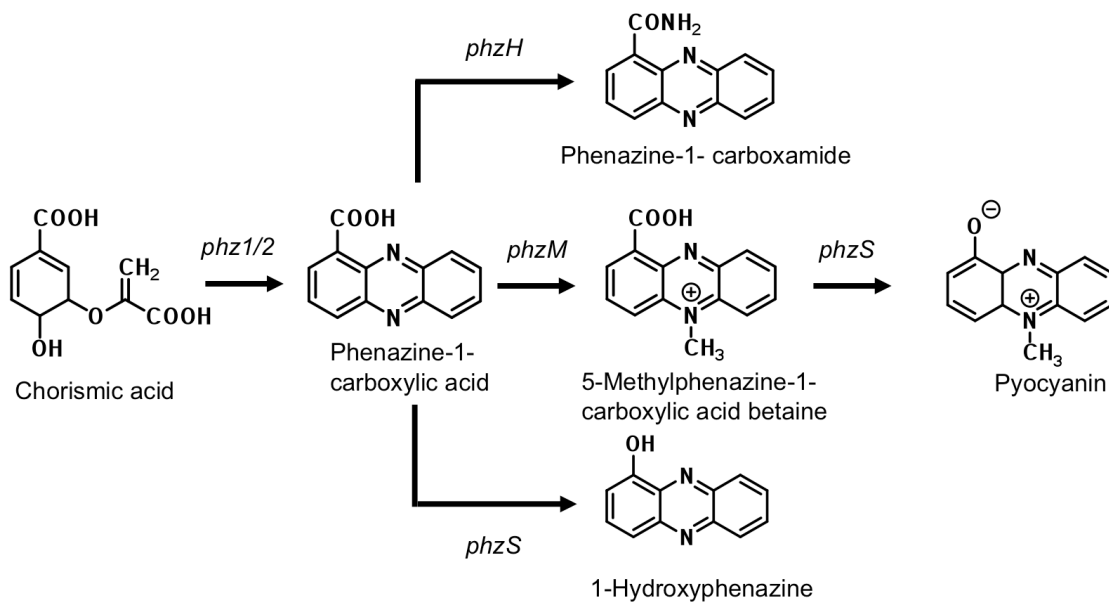

Figure S4.1. Phenazine biosynthetic pathways in *Pseudomonas aeruginosa*. Chorismic acid is transformed into phenazine-1-carboxylic acid via two homologous *phzA1-G1* and *phzA2-G2* operons (*phz1/2*). This phenazine is subsequently converted to phenazine-1-carboxamide, 5-methylphenazine-1-carboxylic acid betaine, 1-hydroxyphenazine and pyocyanin by the phenazine-modifying genes *phzH*, *phzM*, and *phzS*.[6]
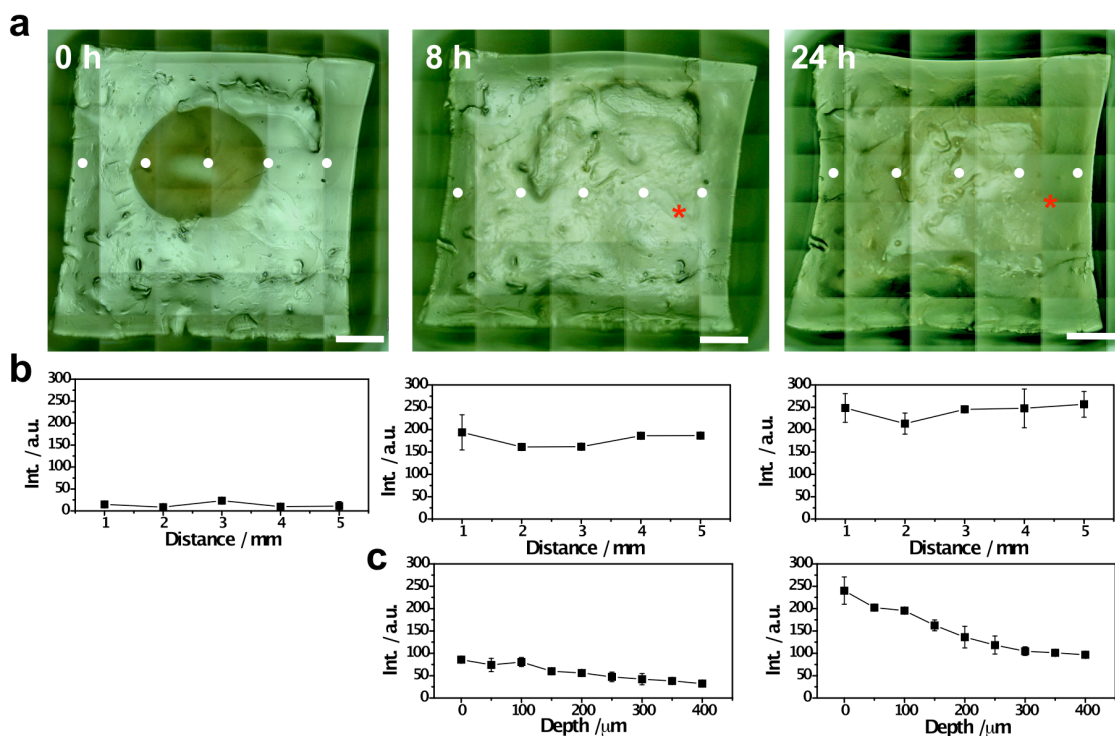
Figure S4.2. Time-evolution analysis of pyocyanin secretion by *P. aeruginosa* PA14 colony-biofilms grown on Au@pNIPAM hydrogels. a) Optical microscopy images of the bacterial colony-biofilm (scale bar: 1 mm). The dark round area in the picture of the hydrogel at time 0 corresponds to the bacterial inoculum. b) SERRS intensities (at 418 cm^{-1}) measured at the places indicated with white dots and plotted as a function of distance from the left edge. The error bars show the standard deviation from two different measurements. SERRS measurements of colony-biofilms were performed using a 785 nm laser line for 10 s at a maximum power at the sample of 0.91 kW/cm^2, with a 20x objective c) SERRS intensities (at 418 cm^{-1}) measured at the places indicated with asterisks and plotted as a function of the depth from the surface. The conditions for SERRS measurements were the same as above.
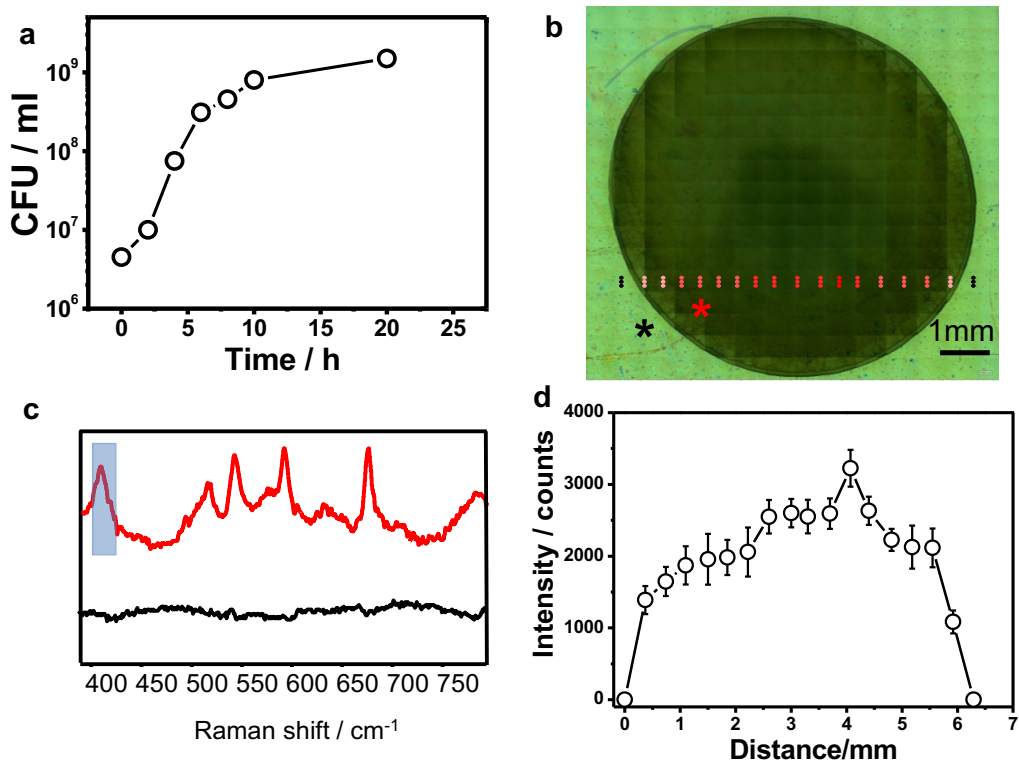
14

Figure S4.3. *In situ* detection of pyocyanin secreted by *P. aeruginosa* PA14 biofilm grown on mesostructured Au@TiO$_2$ substrate. **a**) Graphical representation of viable bacteria (CFU/mL) quantified over time. **b**) Optical image of a *P. aeruginosa* PA14 culture grown as a droplet on the mesostructured Au@TiO$_2$ substrate obtained with the Raman microscope (5× objective). **c**) SERS spectra recorded outside and inside the bacterial culture at the asterisks indicated in **b**. **d**) Graphic representation of the SERS intensity (418 cm^{-1}) recorded at the dots shown in **b** as a function of the distance. All measurements used 785 nm laser and 5× objective.
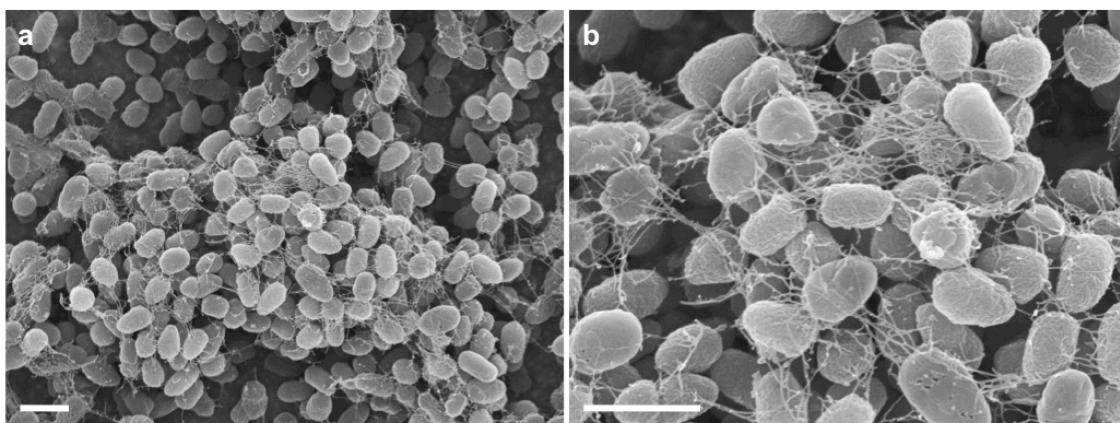

Figure S4.4. Representative SEM images of *P. aeruginosa* PA14 micro-colonies grown on mesostructured Au@TiO$_2$ substrates at different magnifications. Scale bar: 1 μm.
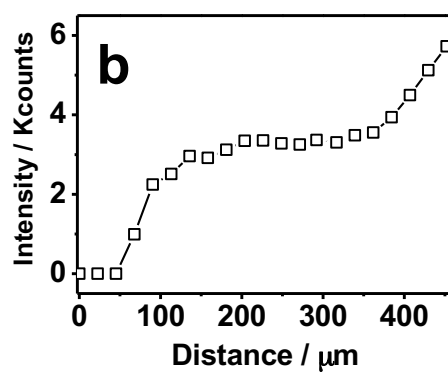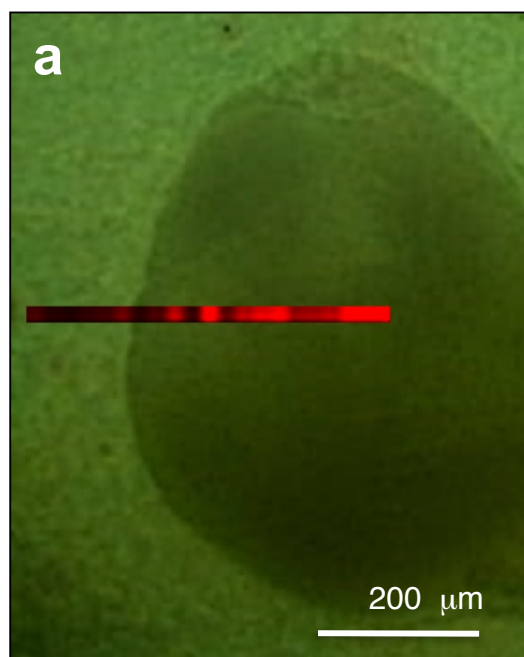
Figure S4.5. *In situ* **detection of pyocyanin secreted by** *P. aeruginosa* **PA14 colony biofilm grown on LB agar layered mesostructured Au@TiO₂ substrate. a**) Optical image of a colony of *P. aeruginosa* grown on mesostructured Au@TiO₂ substrate coated with LB agar (0.75%) and superimposed SERS mapping (418 cm⁻¹) of pyocyanin obtained with a 20× objective. **b**) Graphic representation of the relative intensity of pyocyanin measured in **a** versus the distance from the edge.
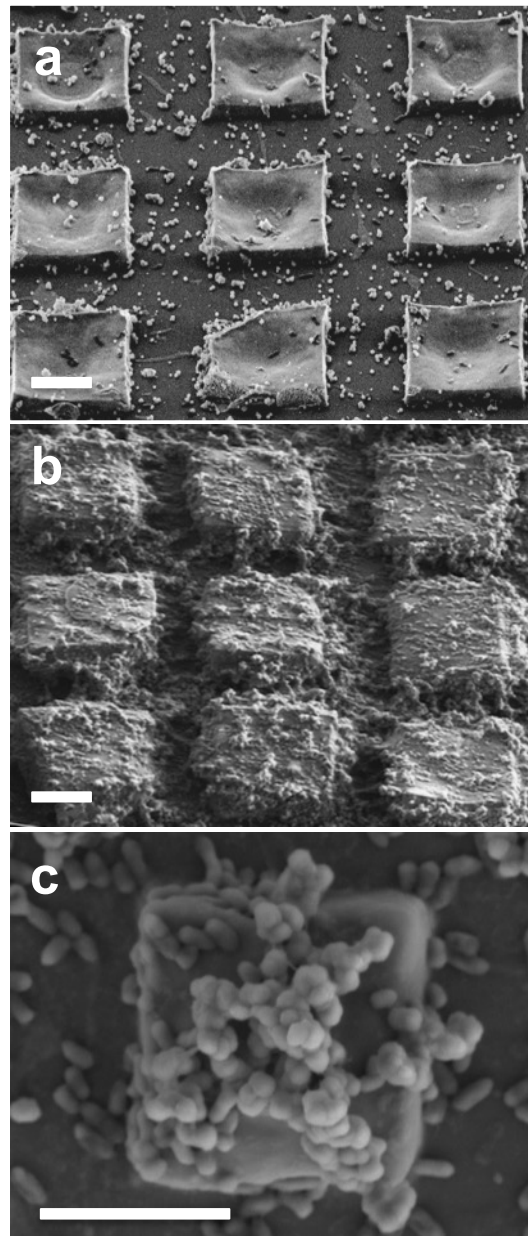
Figure S4.6. Representative SEM images of *P. aeruginosa* PA14 microcolonies grown on micropatterned Au@SiO$_2$ substrates acquired at different growth times; 3 h **a**) and 20 h (**b** and **c**). Scale bars: 10 µm (**a**, **b**) and 5 µm (**c**).

Table S4.1. *P. aeruginosa* **strains used in this study**

P. aeruginosa strain	Characteristics	Reference
PA14	Clinical isolate UCBPP-PA14	[7]
PA14 Δ*phz1/2*	Deletion of *phzA1-G1* and *phzA2-G2 operons*	[8]
PA14 *phzH*	Transposon insertion mutant ID: 39981	[9]
PA14 *phzM*	Transposon insertion mutant ID: 40343	[9]
PA14 *phzS*	Transposon insertion mutant ID: 44099	[9]

References

1.   Frisch M. J., et al. Gaussian 09. Wallingford, CT, USA: Gaussian, Inc.; 2009.

2.   Jamroz M. H. Vibrational energy distribution analysis (VEDA): Scopes and limitations. *Spectrochim Acta A* **114,** 220-230 (2013).

3.   Siebert F., Hildebrandt P. Theory of Infrared Absorption and Raman Spectroscopy in Vibrational Spectroscopy in Life Science Wiley-VCH Verlag GmbH & Co. KGaA, 2009.

4.   Hildebrandt P., Stockburger M. Surface-Enhanced Resonance Raman-Spectroscopy of Rhodamine-6g Adsorbed on Colloidal Silver. *J. Phys. Chem.* **88,** 5935-5944 (1984).

5.   Mavrodi D. V., et al. Functional analysis of genes for biosynthesis of pyocyanin and phenazine-1-carboxamide from Pseudomonas aeruginosa PAO1. *J Bacteriol* **183,** 6454-6465 (2001).

6.   Jimenez P. N., et al. The Multiple Signaling Systems Regulating Virulence in Pseudomonas aeruginosa. *Microbiol. Mol. Biol. Rev.* **76,** 46-65 (2012).

7.   Rahme L. G., et al. Common Virulence Factors for Bacterial Pathogenicity in Plants and Animals. *Science* **268,** 1899-1902 (1995).

8.   Dietrich L. E. P., et al. The phenazine pyocyanin is a terminal signalling factor in the quorum sensing network of Pseudomonas aeruginosa. *Mol Microbiol* **61,** 1308-1321 (2006).

9.   Liberati N. T., et al. An ordered, nonredundant library of Pseudomonas aeruginosa strain PA14 transposon insertion mutants. *Proc. Natl. Acad. Sci. USA* **103,** 2833-2838 (2006).